Journal of Materials Chemistry A

ROYAL SOCIETY OF CHEMISTRY

PAPER

View Article Online
View Journal

Cite this: DOI: 10.1039/d4ta01354a

Graphene triggered catalytic attack on plastic waste produces graphitic shell encapsulation on cobalt nanoparticles for ferromagnetism and stable Li^+ ion storage†

Manikandan Palanisamy,*[ab] Ramakrishnan Perumal,[c] Di Zhang,[d] Haiyan Wang,[d] Olga Maximova,[e] Leonid Rokhinson[e] and Vilas G. Pol*[a]

Plastic materials, *viz.*, Ziploc bags (polyethylene) and packing foam (polystyrene) produce graphitic shell encapsulated cobalt nanoparticles by catalytic microwave deconstruction in 2 minutes. The phase purity is confirmed as cubic crystalline, having graphitic carbon with core–shell architecture recognized by a D-band at 1330 cm^{-1} and G-band at 1575 cm^{-1}, attributed to the calculated specific surface area of 39 $m^2\ g^{-1}$ for Co-GNP-ZipC, 19 $m^2\ g^{-1}$ for Co-GNP-FmC and 47 $m^2\ g^{-1}$ for pristine Co-GNP. Transmission electron microscopic results reveal graphitic shell encapsulation, 20 nm cobalt nanoparticles, carbon lattice fringes, and crystalline cobalt's ring patterns having bright diffraction spots. The magnetization *M vs. H* and magnetic susceptibility χ *vs. T* of pristine Co-GNP, Co-GNP-ZipC, and Co-GNP-FmC materials show the ferromagnetism of cobalt nanoparticles. Kinetic studies of the graphitic core–shell architecture exhibit an additional charge storage buildup and three reversible redox peaks, attributed to (de)insertion in the trace amount of amorphous CoO, conversion reaction of CoO to Co and Li_2O and Li^+ ion (de) intercalation in graphitic shell encapsulated carbon. The plastic waste-derived composite materials deliver a reversible capacity of 377 mA h g^{-1} for Co-GNP-ZipC and 509 mA h g^{-1} for Co-GNP-FmC at the 250th cycle compared to the pristine Co-GNP material (<1 mA h g^{-1}), as a superior Li^+ ion storage material.

Received 28th February 2024
Accepted 21st June 2024

DOI: 10.1039/d4ta01354a

rsc.li/materials-a

1. Introduction

Plastics are widely used in all applications and have proliferated over the past half-century, especially the ubiquitous polyethylene, polypropylene, and polystyrene, which are discarded at the highest rate after their use becoming landfill waste and an environmental burden.[1–4] The increased volume of plastic waste has created a global issue, since these materials release environmentally harmful gaseous hydrocarbons (CH_4, C_2H_2, and C_3H_8, *etc.*), SO_2, SO_3, CO, CO_2, *etc.*, during their decomposition process.[5] To tackle this problem, researchers have developed multifunctional approaches to convert plastic waste into value-added products such as hydrocarbon fuel,[6] hydrogen (H_2),[7] carbon nanotubes (CNTs)[8] and amorphous carbon.[9–11] Thus, the plastic waste is converted into H_2 by solar-driven processes and the plastic waste's monomer, *viz.*, formate, acetate, pyruvate, *etc.*, is regenerated.[12,13] Research studies have further extended to fast and continuous pyrolysis-enhanced steam reforming systems for continuous H_2 production from plastic wastes.[14–16] Significantly, the pyrolysis–catalytic gasification of waste plastics resulted in the co-production of H_2 and CNTs using bifunctional (Ni–Fe) and tertiary catalysts (Ni–Mn–Al, Ni–Ca–Al, Ni–Ce–Al and Ni–Zn–Al).[17–20]

However, most of the research and development of plastic waste towards the production of H_2, CNTs and organic products is associated with expensive techniques, consisting of multi-stage processing steps.[7,8,12–20] The conversion of plastic wastes into value-added carbon is not a direct and easy process with either high-temperature treatment in a reactor[14–20] or extended treatment in acid.[11,21] Hence, a time- and energy-savvy facile route, *viz.*, microwave irradiation, is one of the best choices for the conversion of plastic waste into value-added products. In this technique, the electromagnetic heating of microwave-absorbing materials is rapid having high dielectric loss

[a]*Davidson School of Chemical Engineering, Purdue University, West Lafayette, IN 47907, USA. E-mail: manikandancy@gmail.com; vpol@purdue.edu*

[b]*Department of Mechanical, Aerospace, and Biomedical Engineering, University of Tennessee, Knoxville, TN 37996, USA. E-mail: mpalanis@utk.edu*

[c]*Department of Mechanical Engineering, SRM TRP Engineering College, Tiruchirappalli, Tamilnadu, 621105, India*

[d]*Materials Engineering/Electrical and Computer Engineering, Purdue University, West Lafayette, IN 47907, USA*

[e]*Department of Physics and Astronomy, Purdue University, West Lafayette, IN 47907, USA*

† Electronic supplementary information (ESI) available. See DOI: https://doi.org/10.1039/d4ta01354a

tangents, and the microwave energy, transformed immediately into heat throughout the sample, results in effective microwave heating.[22–24] Graphene has the unique characteristics of excellent electromagnetic conduction and high thermal conductivity (5300 W m^{-1} K^{-1}) compared to traditional carbon materials, *viz.*, active carbon and graphite.[25–30] Thus, graphene has been used as a microwave absorbing material, and it has also been used to develop graphite nanoplatelets/epoxy composites,[31] strontium ferrite–carbon black–nitrile latex composites,[32] graphene coated/Fe nanocomposites,[33] and frequency selective radar absorbing materials[34] for applications such as shields or to absorb the electromagnetic radiation and minimize the radar-cross section of military vehicles (ships, tanks, and aircraft).

Moreover, multifunctional electrocatalysts (CoO@Co comprising a core–shell structure) have been synthesized by an environment-friendly and cost-effective microwave irradiation technique using microwave absorbing graphite oxide materials for the oxygen evolution reaction (OER), oxygen reduction reaction (ORR), and hydrogen evolution reaction (HER).[35,36] Highly efficient metallic electrocatalysts, *viz*, G–Ni–Fe, G–Ni–Co, G–Co–Fe and G–Ni–Co–Fe, have been developed with graphitic shell encapsulation by a two-step process of a sol–gel method and a carbothermal route for the applications of the OER, ORR, and HER.[37] The core–shell architecture and the graphitic shell encapsulation on the surface of the nanoarchitecture materials play significant roles in energy storage applications.[35–37] Since the shell caging covers the metal nanoparticles completely by a few nanometers thickness (2–5 nm), no agglomeration or clusters occur, enabling a barrier between the highly reactive core-active nanoparticles and electrolyte solution to prevent unwanted chemical and electrochemical reactions.[37] In particular, the graphitic shell encapsulation prevents the metal nanoparticle's phase transformation during electrolysis and protects the highly active metal nanoparticle from oxidative corrosion reactions under its harsh environmental conditions.[37–40] The core–shell architecture is very promising for the applications of lithium-ion batteries (LIBs), specifically for metal-based anodes such as Co,[41,42] Si,[43] Sb,[44] Sn,[45] Sn–Ni–Ti,[46] Co_3O_4,[47] Sb_2O_3,[44,48] and SnO_2 (ref. 49), and could achieve high specific capacity at high-rate cycling. The literature shows that the metal nanoparticles, composite alloy, and pristine metal oxide anodes are highly reactive with an electrolyte solution, consuming more Li^+ ions from the cathode, large initial irreversibility capacity loss, and rapid capacity decay during alloying–dealloying reactions.[41–49] Thus, metal based anodes suffer from apparent volume expansion during conversion reaction of pristine Si and Sn metal anodes (>300%), alloying dealloying of composite alloy anodes, and the simultaneous process of conversion, intercalation–deintercalation reactions of metal oxide anodes, leading to mechanical strain, electrode disintegration, and poor electronic conductivities, resulting in capacity-fade during discharge/charge cycling studies.[41,43,45,46]

From the known literature, core–shell architecture has been developed by conventional chemical vapor deposition, atomic layer deposition, polymer coating coupled thermal treatment, solvothermal coupled thermal treatment, ball milling and high-temperature pyrolytic methods.[50–52] Nevertheless, the graphitic shell encapsulation produced by microwave irradiation can be a distinctive environment-friendly and cost-effective method compared to the other methods. Significantly, the catalytic deconstruction of plastic waste (polyethylene, polypropylene, and polystyrene) by microwave irradiation produced multi-walled carbon nanotubes (predominantly) and H_2 (55.6 mmol g^{-1}) in a simple and ultrafast one-step process (30–90 s).[53] Moreover, the research and development of conversion of plastic waste into graphitic shell encapsulation on metal anodes by microwave irradiation technology will be a superior ultrafast technique for the creation of core–shell architecture with reduced toxic gas emissions of hydrocarbons (CH_4, C_2H_2 and C_3H_8 *etc.*), SO_2, SO_3, CO, CO_2, *etc.*

In this study, we report polyolefin plastic waste, *viz.*, polyethylene and polystyrene catalytically deconstructed by a graphene triggered electromagnetic catalytic reaction into graphitic shell encapsulation on cobalt nanoparticles to achieve ferromagnetism and stable Li^+ ion storage for lithium-ion batteries (LIBs) by a time- and energy-savvy facile route using a microwave irradiation technique. The plastic waste derived graphitic shell encapsulated cobalt nanoparticles are characterized by powder X-ray diffraction (XRD) and Raman spectroscopic analyses. The core–shell architecture was confirmed by advanced transmission electron microscopic (TEM) analysis with elemental mapping. The graphitic shell encapsulated cobalt nanoparticles exhibited ferromagnetism, revealed capacity-fade abated cycling performance, and delivered higher discharge- and charge capacities of 509/506 mA h g^{-1} at the 250th cycle compared to the conventional route (25/24 mA h g^{-1}, without plastic waste). The results of this work can be used to create advanced LIB materials using microwave irradiation of common plastics.

2. Results & discussion

2.1. Structural characterization of plastic waste derived graphitic cobalt nanoparticles

The process used to create graphitic shell encapsulation on cobalt nanoparticles for stable Li^+ ion storage is shown in Fig. 1. In this study, we achieved graphitic shell encapsulation on cobalt nanoparticles using plastic waste in 2 minutes, much faster than conventional techniques.[50–52] The landfill plastic wastes, *viz.*, Ziploc bags (polyethylene, Fig. 1a), and food packing boxes and packing foam materials (polystyrene, Fig. 1b) were mixed with cobalt acetate in separate round bottom flasks (Fig. 1c–g). The Ziploc bags were cut into smaller sizes (Fig. 1c) and the polystyrene pieces (Fig. 1d) dissolved in acetone with natural evaporation (Fig. 1e). Then, the mixture of the plastic wastes and the cobalt acetate in a separate round bottom flask (Fig. 1f and g) was blended with 43 mg of microwave-absorbing graphene nanoplatelets (GNPs). The blended mixture was then irradiated with microwaves for 2 minutes (Fig. 1h). Simultaneous reactions of GNP microwave absorption, cobalt acetate decomposition, and catalytic plastic waste degradation (Fig. 1i–k) produced graphitic shell encapsulated cobalt nanoparticles, as shown schematically in Fig. 1l–o. The products derived were

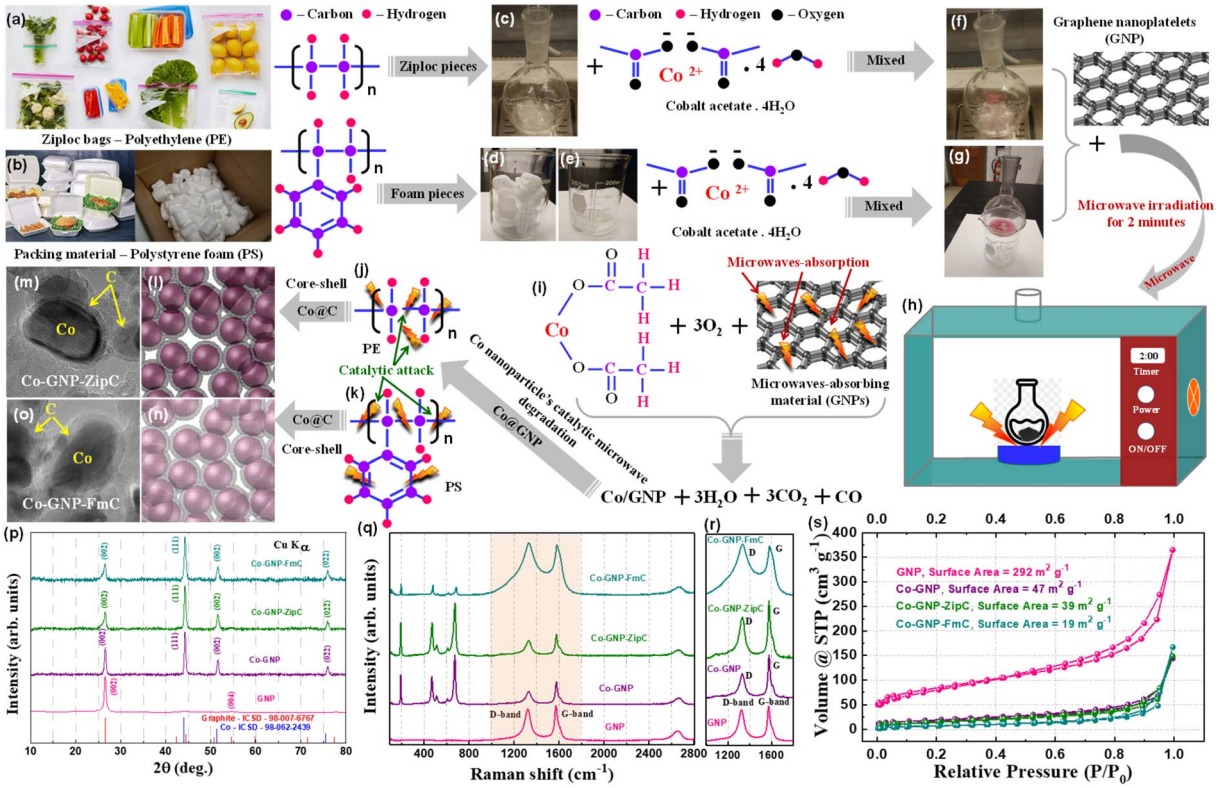

Fig. 1 Plastic waste built graphitic core–shell architecture and the structural characterization: photographs of landfill plastic wastes: (a) Ziploc bags (polyethylene), (b) food packing boxes and packing foam materials (polystyrene), (c) polyethylene Ziploc bags cut into smaller sizes, (d) polystyrene pieces, dissolved (e) in acetone and allowed to evaporate naturally, mixture of (f) Ziploc bag pieces with cobalt acetate, (g) packing foam with cobalt acetate, the mixture blended with microwave absorbing graphene nanoplatelets (h) irradiated by microwaves for 2 minutes, (i) schematics of the simultaneous reactions of microwave absorption by GNPs and cobalt acetate decomposition, catalytic attack of (j) polyethylene degradation, (k) polystyrene degradation, (l) schematized core–shell structure for polyethylene, (m) polyethylene derived graphitic shell encapsulated cobalt nanoparticles, (n) core–shell structure schematics for polystyrene, (o) polystyrene derived graphitic shell encapsulated cobalt nanoparticles, (p) powder X-ray diffraction patterns of pristine Co-GNP (purple), plastic waste derived Co-GNP-ZipC (green), Co-GNP-FmC (cyan) materials, standard patterns of graphite ICSD# 98-007-6767 (red) and Co metal ICSD# 98-062-2439 (blue), (q) Raman spectroscopy measurements of plastic waste derived materials Co-GNP-ZipC (green), Co-GNP-FmC (cyan), Co-GNP (purple) and GNP (pink), (r) the confirmed D-band and G-band for the presence of graphitic carbon, and (s) BET specific surface area measurement of Co-GNP-ZipC (green), Co-GNP-FmC (cyan), Co-GNP (purple) and GNP (pink).

labelled Co-GNP-ZipC (polyethylene's plastic waste – Ziploc bag) and Co-GNP-FmC (polystyrene's plastic waste – foam), confirming the graphitic shell encapsulation on the cobalt nanoparticles as indicated by carbon (C) and cobalt (Co) in Fig. 1m and o. Alternatively, the cobalt acetate and GNP mixed without the plastic waste and treated with microwave irradiation for 2 minutes yielded a Co-GNP product. Thermogravimetric analysis was performed on the mixture of cobalt acetate and graphene for the pristine sample which yielded the product of Co-GNP material, as given in Fig. S1a.† A thermogravimetric curve revealed the dehydration of adsorbed water molecules (<120 °C), a weight loss of 38% between 100 and 320 °C for the acetate decomposition reaction; further reduction reaction of CoO to Co metal nanoparticles in the presence of graphene at 600 to 650 °C results in a 4% weight loss.[52]

Powder X-ray diffraction (XRD) patterns of plastic waste derived Co-GNP-ZipC (green), Co-GNP-FmC (cyan) and pristine Co-GNP (purple, without plastic waste) materials were investigated using GNP XRD (pink), and compared to the standard patterns of Co, ICSD# 98-062-2439 (blue) and graphite, ICSD# 98-007-6767 (red), as shown in Fig. 1p. The predominant XRD peaks at 44.2°, 51.5° and 75.9° (2θ) represent the formation of the cubic crystal structure of metallic Co, well-indexed with the Co planes (111), (002) and (022), without any other oxide impurity phases, *viz.*, CoO and Co_3O_4,[37,54] even though the synthesis was carried out in an air atmosphere. The residual XRD peak at 26.5° (2θ) perfectly matched with the GNP peak (002), confirming the presence of GNPs in the products,[28,55,56] as given in Fig. 1p. The graphitic nature of the derived composite materials Co-GNP-ZipC (green), Co-GNP-FmC (cyan) and Co-GNP (purple) was examined by Raman spectroscopy measurements with the pristine GNP sample (pink), as shown in Fig. 1q. The detected D-band at 1330 cm^{-1} and G-band at 1575 cm^{-1} confirm the presence of carbon with graphitic nature (Fig. 1r) and the obtained Raman spectra well-matched with the literature reports.[33,43,57] The D-band of Co-GNP-ZipC (green) and Co-GNP-FmC (cyan) materials appeared at 1330 cm^{-1} with broad comparison to the pristine Co-GNP material (pink),

representing more presence of sp^3 carbon corresponding to the defective graphitic structure.[33,43,57] The degree of graphitization ($R = I_D/I_G$) was estimated from the ratio of D-band and G-band intensities for the GNPs (0.9), Co-GNP (0.56), Co-GNP-ZipC (0.7) and Co-GNP-FmC (1) materials, as listed in Table S1.† The degree of disordered graphitic carbon increases in the order of Co-GNP < Co-GNP-ZipC < Co-GNP-FmC, revealing that polystyrene packing foam produces more carbon defects, as shown in Fig. 1r.

Subsequently, the surface characteristics of Co-GNP-ZipC (green), Co-GNP-FmC (cyan) and pristine Co-GNP samples were examined by Brunauer–Emmett–Teller (BET) specific surface area measurement, evaluated with the N_2 adsorption–desorption isotherm curves, as shown in Fig. 1s.† The N_2 adsorption–desorption isotherm curves of plastic waste derived Co-GNP-ZipC (green) and Co-GNP-FmC (cyan) materials show the slope and flat plateaus at 0 to 1 P/P_0 values and revealed the H3 and H4-hysteresis loops, indicating the presence of micropores (H3-hysteresis loop) and mesopores (H4-hysteresis loop).[58,59] However, the decreased angle of the slope and the elevated flat plateaus confirm the mesoporous characteristics compared to the micropores, and the observed plateaus closely match with the graphitic N_2 adsorption–desorption isotherm curve.[42,43,60] Furthermore, the absence of strong N_2 adsorption at less than 0.1 relative pressure (Fig. 1s†) confirms the reduced micropore-filling characteristics of plastic waste derived Co/C composite materials, in contrast to the hard carbon anode.[60] The measured BET-specific surface area of the plastic waste derived composite materials was 39 $m^2\ g^{-1}$ for Co-GNP-ZipC (green), 19 $m^2\ g^{-1}$ for Co-GNP-FmC (cyan) and 47 $m^2\ g^{-1}$ for pristine Co-GNP, which are almost six times less than the GNP surface area, 292 $m^2\ g^{-1}$ (Fig. S1b†), and close to graphitic carbon and Co metal. Thus, the structural characteristic studies of the plastic waste derived composite materials confirmed the presence of graphitic carbon and Co nanoparticles, which would enable stable Li^+ ion storage.

2.2. Elucidation of ultrafast graphitic shell encapsulation on cobalt nanoparticles

Landfill plastic waste such as Ziploc bags (polyethylene), and food packing boxes and packing foam materials (polystyrene) produced ultrafast graphitic shell encapsulation on cobalt nanoparticles in 2 minutes by catalytic microwave degradation, confirmed by the transmission electron microscopic technique (TEM). The surface morphological TEM results of pristine Co-GNP (Fig. 2a–e), Co-GNP-ZipC (Fig. 2f–j) and Co-GNP-FmC (Fig. 2k–o) materials are given in Fig. 2, 3, and S2.† From the bright-field TEM images, it can be clearly seen that the plastic waste derived Co-GNP-ZipC (Fig. 2f, g, S2d and e†) and Co-GNP-FmC (Fig. 2k, l, S2g and h†) materials showed cluster morphology, comprising cobalt particles covered completely with carbon, as a matrix. In contrast, the pristine Co-GNP material revealed agglomerated morphology, containing cobalt and graphene nanoplatelets, as shown in Fig. 2a, b, S2a and b.† Also, some of the cobalt nanoparticles are exposed directly without the carbon matrix and the graphene nanoplatelets existed individually, as indicated in Fig. 2b–d. Further investigation of the plastic waste derived materials revealed the core–shell architecture, as shown in Fig. 2h (Co-GNP-ZipC) and Fig. 2m (Co-GNP-FmC). The ultrafast core–shell architecture was attained in 2 minutes compared to the literature methods on core–shell morphologies developed by conventional routes, *viz.*, chemical vapor deposition, atomic layer deposition, polymer coating coupled thermal treatment, solvothermal coupled thermal treatment, ball milling and high-temperature pyrolytic methods.[50–52] Moreover, the core–shell architecture's carbon matrix revealed lattice fringes, recognized as a graphitic nature with the thickness of ~2 nm, encapsulated completely on cobalt nanoparticles (~20 nm) confirmed by high-resolution transmission electron microscopic (HRTEM) images, as defined in Fig. 2i (Co-GNP-ZipC) and Fig. 2n (Co-GNP-FmC). The obtained ultrafast graphitic shell encapsulated cobalt nanoparticle morphology perfectly matched with the sol–gel method-derived graphitic shell encapsulation on cobalt nanoparticles, used as an efficient electrocatalyst.[37] On the other hand, the pristine Co-GNP material revealed GNP sheets and cobalt particles separately without any core–shell architecture, as depicted in Fig. 2d and S2c.† Moreover, it is pertinent to note that the catalytic microwave degradation of landfill plastic waste produced carbon nanotubes (CNTs) with the thickness of 10 nm in 2 minutes, as confirmed in Fig. S2e and f† for Co-GNP-ZipC and Fig. S2h and i† for Co-GNP-FmC materials, though the synthesis was carried out in an air atmosphere. The obtained carbon nanotube dimension and the morphologies are corroborated with the CNT report, derived by a two-step pyrolysis and gasification process.[53] The selected area electron diffraction (SAED) analyses of pristine Co-GNP (Fig. 2e), Co-GNP-ZipC (Fig. 2j) and Co-GNP-FmC (Fig. 2o) materials revealed ring patterns with bright diffraction spots corresponding to the highly crystalline nature of cobalt nanoparticles[35] and agreed with the (111) and (002) crystal planes at 44° and 51.5° (2θ), as given in Fig. 1p. Thus, the presence of highly crystalline cobalt nanoparticles and the carbon lattice fringes confirmed the existence of ultrafast graphitic shell encapsulated cobalt nanoparticles, as schematized in Fig. 1l and m (Co-GNP-ZipC) and Fig. 1n and o (Co-GNP-FmC), and the results corroborated with the literature reports of the core–shell architecture developed by multiple processing steps.[35–38,54] Besides, high-angle annular dark field (HAADF) images of pristine Co-GNP (Fig. 3a), Co-GNP-ZipC (Fig. 3f) and Co-GNP-FmC (Fig. 3k) materials, and the simultaneous elemental mapping analyses confirmed the presence of cobalt (red) and carbon (green) in pristine Co-GNP (Fig. 3b and c), Co-GNP-ZipC (Fig. 3g and h) and Co-GNP-FmC (Fig. 3l and m) materials. The presence of cobalt nanoparticles and GNPs associated with the cobalt and graphite phases was confirmed by powder XRD patterns, as given in Fig. 1p and literature reports.[37,54,61] Also, additional oxygen existence in pristine Co-GNP (Fig. 3d), Co-GNP-ZipC (Fig. 3i) and Co-GNP-FmC (Fig. 3n) materials was attributed to the GNPs (Fig. S3†), containing trace amounts of oxygen, as confirmed in Fig. S3e and f.† Ultimately, the presence of cobalt, carbon and oxygen elements was quantified by the spectrum of TEM energy dispersive X-ray analysis, as given in Fig. 3e (pristine Co-GNP), Fig. 3j (Co-GNP-ZipC) and

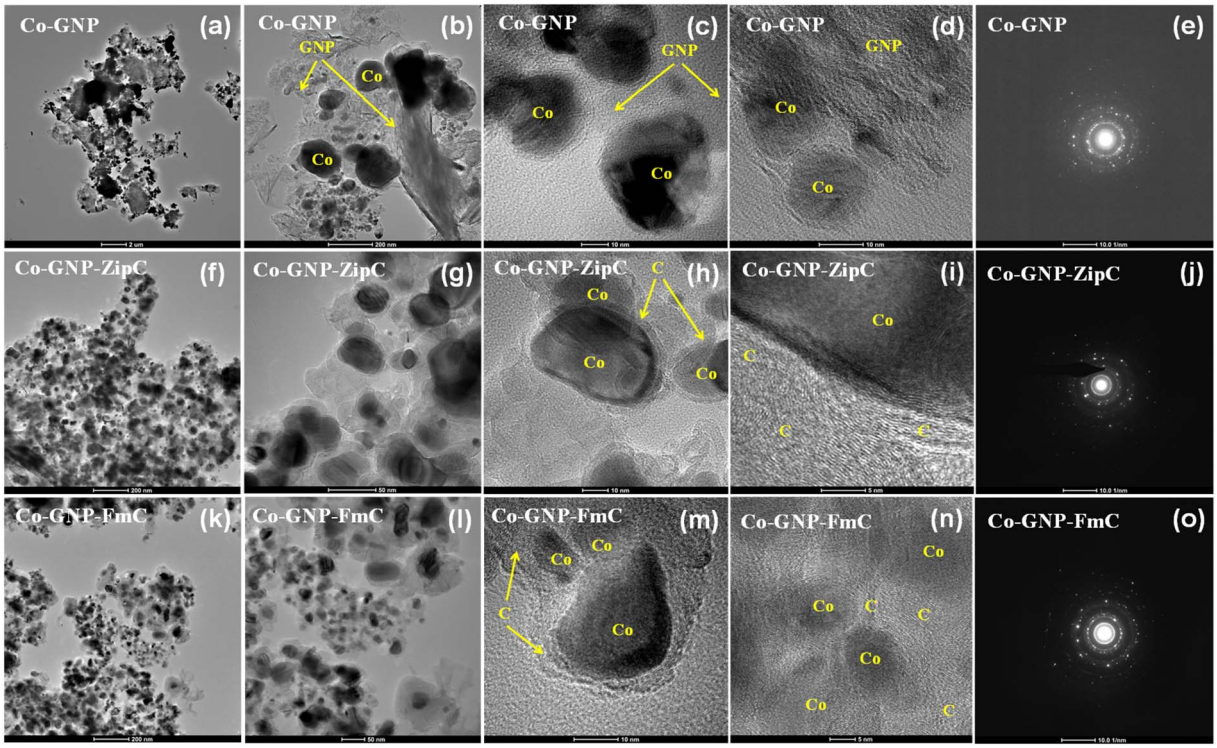

Fig. 2 Transmission electron microscopic images of graphitic shell encapsulated cobalt nanoparticles: (a) pristine Co-GNP, (b) containing cobalt and graphene nanoplatelets, (c) cobalt nanoparticles exposed without the carbon matrix, (d) the GNP sheets and the cobalt nanoparticles existed individually, (e) SAED of pristine Co-GNP; (f) morphological image of the Co-GNP-ZipC material, (g) cobalt nanoparticles with the carbon matrix, (h) polyethylene derived graphitic carbon encapsulated cobalt nanoparticles, (i) carbon matrix of the core–shell architecture revealed lattice fringes, (j) SAED of Co-GNP-ZipC; and (k) morphological image of the Co-GNP-FmC material, (l) cobalt nanoparticles with carbon, (m) polystyrene derived graphitic carbon encapsulated cobalt nanoparticles, (n) the core–shell architecture's carbon matrix revealed lattice fringes, (o) SAED of Co-GNP-FmC.

Fig. 3o (Co-GNP-FmC), and confirmed 86% of high-value carbon in plastic waste derived Co-GNP-ZipC and Co-GNP-FmC materials compared to the pristine Co-GNP material (70% carbon). The additional 16% of carbon in the plastic waste-derived materials was associated with the "conversion" of landfill plastic waste, *viz.*, polyethylene (Ziploc bags) and polystyrene (food packing boxes and packing foam) into "high-value-added carbon". Thus, graphitic shell encapsulation on cobalt nanoparticles was built by plastic waste in 2 minutes and can be used for ferromagnetism and stable Li^+ ion storage.

2.3. Ferromagnetism of graphitic shell encapsulated cobalt nanoparticles

The magnetic field dependence of magnetization M *vs.* H and temperature dependence of magnetic susceptibility χ *vs.* T of pristine Co-GNP, Co-GNP-ZipC and Co-GNP-FmC were studied using a Quantum Design MPMS SQUID magnetometer in DC mode. The temperature dependence of magnetic susceptibility χ *vs.* T measured in the temperature range of 1.8–300 K at 1000 Oe does not show any feature at $T = 291$ K corresponding to the Néel temperature of antiferromagnetic phase transition in CoO. The latter implies no significant presence of the CoO phase in the samples pristine Co-GNP, Co-GNP-ZipC and Co-GNP-FmC which agrees with the data from phase structural analysis, as given in Fig. 1p. To confirm the ferromagnetic behavior of the studied samples, the temperature dependences of magnetic susceptibility χ *vs.* T were captured in field cooled (FC) and zero-field-cooled (ZFC) modes in a temperature range of 300–1.8 K at 1000 Oe (Fig. 4a). The ZFC magnetic susceptibility curve of all samples does not show any maxima and decreases with temperature in all measured temperature ranges. The FC and ZFC dependencies for both samples remain separate up to 300 K which indicates a ferromagnetic material. The field dependencies of magnetization were measured at 300 K in the range of magnetic fields −30000 Oe to 30 000 Oe and evidence the ferromagnetic behavior of the pristine Co-GNP, Co-GNP-ZipC and Co-GNP-FmC materials, as described in Fig. 4b. The obtained values of remanent magnetization, M_R, and saturation of magnetization, M_s, are $M_s = 91$ emu g^{-1}, $M_R = 7$ emu g^{-1} for pristine Co-GNP, $M_s = 48$ emu g^{-1} and $M_R = 8.4$ emu g^{-1} for Co-GNP-ZipC, $M_s = 47$ emu g^{-1} and $M_R = 11.4$ emu g^{-1} for Co-GNP-FmC materials. The coercive fields of $H_c = 186$ Oe (Co-GNP), $H_c = 370$ Oe (Co-GNP-ZipC) and $H_c = 449$ Oe (Co-GNP-FmC) exceed the coercivity for bulk cobalt, $H_c = 40$ Oe.[62,63] The theory predicts coercivity H_c depending on the grain size as $H_c \sim D^{-1}$, for particle size $D > D_c$, and decreases as $H_c \sim D^6$ for particles of smaller size, $D < D_c$, where D_c is the critical grain size, and $D_c =$ 15 nm for cobalt.[63,64] The TEM studies indicate that sizes of

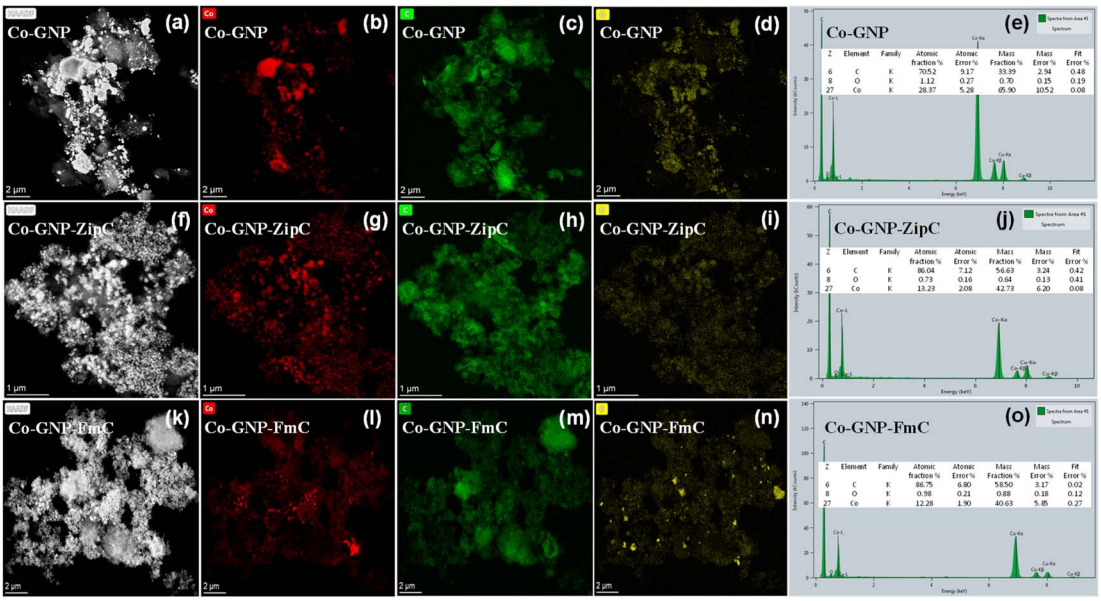

Fig. 3 Simultaneous elemental mapping analyses of pristine and plastic waste derived composite materials: (a) HAADF image of pristine Co-GNP material, simultaneous elemental mapping analyses confirm the presence of (b) cobalt (Co, red), (c) carbon (C, green); and (d) oxygen (O, yellow), (e) the presence of Co, C and O in the pristine Co-GNP material quantified by the spectrum of TEM energy dispersive X-ray analysis; (f) HAADF image of the polyethylene derived Co-GNP-ZipC material, simultaneous elemental mapping analyses confirm the presence of (g) cobalt (Co, red), (h) carbon (C, green); and (i) oxygen (O, yellow), (j) the presence of Co, C and O in the Co-GNP-ZipC material quantified by the spectrum of TEM energy dispersive X-ray analysis; and (k) HAADF of the polystyrene derived Co-GNP-FmC material, simultaneous elemental mapping analyses confirm the presence of (l) cobalt (Co, red), (m) carbon (C, green); and (n) oxygen (O, yellow), (o) the presence of Co, C and O in the Co-GNP-FmC material quantified by the spectrum of TEM energy dispersive X-ray analysis.

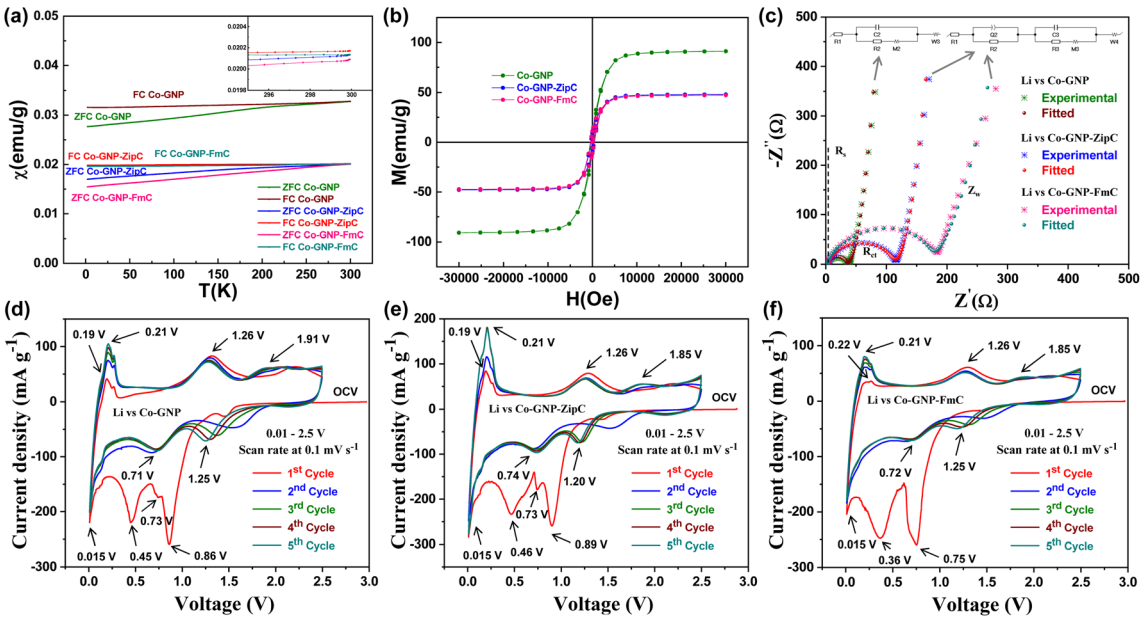

Fig. 4 Magnetic properties and kinetic characteristics of pristine and plastic waste derived composite materials: (a) temperature dependences of magnetic susceptibility χ *vs.* T captured in FC and ZFC modes in a temperature range of 1.8–300 K at 1000 Oe, (b) field dependences of magnetization measured at 300 K in the range of magnetic fields −30000 Oe to 30 000 Oe for the pristine Co-GNP, Co-GNP-ZipC and Co-GNP-FmC materials, confirming ferromagnetic characteristics of cobalt; (c) electrochemical impedance spectroscopic analyses using fabricated lithium cells (Li *vs.* Co-GNP, Li *vs.* Co-GNP-ZipC and Li *vs.* Co-GNP-FmC) in the range of 1 MHz to 25 mHz at 10 mV amplitude; cyclic voltammetric analyses of (d) Li *vs.* Co-GNP (pristine), (e) Li *vs.* Co-GNP-ZipC, and (f) Li *vs.* Co-GNP-FmC lithium cells between 0.01 and 2.5 V at 0.1 mV s^{-1} for 1–5 cycles. The lithium cells assembled with the respective electrode (Co-GNP, Co-GNP-ZipC and Co-GNP-FmC), lithium metal foil (~120 μm thickness), Celgard polypropylene separator and 1 M $LiPF_6$ in EC + DEC (1 : 1 vol%) electrolyte.

nanoparticles formed in Co-GNP, Co-GNP-ZipC and Co-GNP-FmC are larger than the critical value of 15 nm, so the observed ferromagnetic behavior is consistent with morphological analysis. The difference in the coercivity of samples is tentatively associated with the difference in the sizes of nanoparticles in the studied samples, so that on average the size of nanoparticles in the sample Co-GNP is larger than in Co-GNP-ZipC and Co-GNP-FmC materials.

2.4. Electrochemical kinetic studies of graphitic shell encapsulated cobalt nanoparticles

The charge transfer resistance of the plastic waste derived Co-GNP-ZipC and Co-GNP-FmC materials was examined by electrochemical impedance spectroscopic (EIS) studies[42,65,66] using fabricated lithium cells (Li *vs.* Co-GNP-ZipC and Li *vs.* Co-GNP-FmC), and compared with the pristine Co-GNP material (Li *vs.* Co-GNP), as shown in Fig. 4c. EIS spectra of the Co-GNP-ZipC and Co-GNP-FmC materials clearly showed semicircle (experimental data specified in asterisks) features, corresponding to the charge transfer resistance of R_{ct} 115 Ω (Co-GNP-ZipC, blue; combination of R_2, R_3 and Rd_3) and 181 Ω (Co-GNP-FmC, pink; combination of R_2, R_3 and Rd_3), fitted with the complex equivalent circuit of $R_1 + Q_2/R_2 + C_3/(R_3 + M_3) + W_4$ (red, cyan), showing an additional charge storage buildup of Q_2 and R_2 circuit components corresponding to a disordered/ordered graphitic carbon shell on the cobalt nanoparticles. In contrast, the pristine EIS spectrum (Co-GNP, green) showed a low charge transfer resistance of R_{ct} 37 Ω and was fitted with a simple equivalent circuit of $R_1 + C_2/(R_2 + M_2) + W_3$ (maroon) without any other charge buildup. As a result, it was observed that the graphitic shell encapsulation acts as a wall on cobalt metals for the electrochemical kinetic studies and reveals charge storage buildup (Q), which can increase the charge transfer resistance compared to the pristine Co-GNP material, as shown in Fig. 4c. The calculated equivalent circuit component's values are listed in Table S2.† Also, the Nyquist plot comprised an electrolyte solution resistance R_s ~3 Ω for 1 M $LiPF_6$ in EC + DEC (1 : 1 vol%) and a low-frequency Warburg Z_w process (Co-GNP-ZipC and Co-GNP-FmC) associated with high semi-infinite linear diffusion of graphitic shell encapsulated cobalt nanoparticles.[42,66] From the measured EIS results, the ultrafast plastic waste derived Co-GNP-ZipC and Co-GNP-FmC materials can be used for Li^+ ion storage in Li-ion batteries.

The reversible kinetic studies of pristine Co-GNP, Co-GNP-ZipC and Co-GNP-FmC materials were investigated by cyclic voltametric analyses using fabricated lithium cells, *viz.*, Li *vs.* Co-GNP, Li *vs.* Co-GNP-ZipC and Li *vs.* Co-GNP-FmC, assembled with 1 M $LiPF_6$ in EC + DEC (1 : 1 vol%) electrolyte, between 0.01 and 2.5 V at 0.1 mV s^{-1} for 1–5 cycles, as shown in Fig. 4d–f. The cyclic voltametric signals of the pristine Co-GNP (Fig. 4d) and plastic waste derived Co-GNP-ZipC (Fig. 4e) and Co-GNP-FmC (Fig. 4f) materials were associated with the CoO material reported in the literature,[42,47,66–69] though it contained Co nanoparticles and GNPs. Thus, the initial cathodic scan can proceed with the reduction reaction due to the presence of trace impurity functional groups, *viz.*, COOH, CO, O^{2-} and OH^- (located at the surface of GNPs/graphitic carbon),[70] and the formation of nanosized Co–Li–O intermediate cluster[71,72] yields amorphous CoO and Li_2O products[42,47,66–69] with the signature of the first predominant reduction peak appearing at 0.86 V (Fig. 4d), 0.89 V (Fig. 4e), and 0.75 V (Fig. 4f), followed by an electrolyte decomposition reaction and formation of a solid electrolyte interface (SEI).[42,66,68,69] The subsequent reduction peak at 0.73 V was attributed to the trace amount of Li^+ ion insertion of amorphous CoO,[71,72] revealing a sharp reduction peak. The next broad reduction peak at 0.4 V was corroborated with the conversion reaction of CoO to Co and Li_2O products,42,47,66–69 as shown in Fig. 4d–f. Moreover, an additional predominant reduction peak at 0.015 V was observed, which confirms the Li^+ ion intercalation in GNPs (pristine) and graphitic shell encapsulated carbon (Co-GNP-ZipC and Co-GNP-FmC), as given in Fig. 4d–f. Accordingly, initial cyclic voltammograms of pristine (Co-GNP) and plastic waste derived materials (Co-GNP-ZipC and Co-GNP-FmC) exhibited multiple reduction peaks during the initial cathodic scan, associated with the formation of CoO and SEI (eqn (1)), Li^+ ion insertion in trace amounts of amorphous CoO (eqn (3)), conversion reaction of CoO to Co and Li_2O (eqn (3)) and Li^+ ion intercalation in GNPs/graphitic shell encapsulated carbon (eqn (4)).[42,47,66–69,71,72]

$$\text{Co} + \text{GNP/G}(O^{2-},OH^-) + \text{electrolyte decomposition} \rightarrow \text{CoO} + Li_2O + \text{SEI} \quad (1)$$

$$\text{CoO} + xLi^+ + xe^- \leftrightarrow Li_xCoO \quad (2)$$

$$\text{CoO} + 2Li^+ + 2e^- \leftrightarrow \text{Co} + Li_2O \quad (3)$$

$$\text{C(GNP/graphitic shell encapsulation)} + xLi^+ + xe^- \leftrightarrow Li_xC \quad (4)$$

During the anodic scan, the first anodic peak was observed at 0.19/0.22 V (Fig. 4d–f) and confirms deintercalation of Li^+ ion from the GNPs/graphitic shell encapsulated carbon, given in eqn (4). Then, the presence of broad oxidation peaks at 1.26 and 1.91/1.85 V was attributed to the reversible conversion reaction (eqn (3), 1.26 V)[42,47,66–69,71,72] and the Li^+ ion deinsertion of amorphous CoO (eqn (2), 1.91/1.85 V), as indicated in Fig. 4d–f. Notably, the first reduction peak at 0.8 V was observed as an irreversible electrochemical process and disappeared during the anodic scan and upcoming cycles, indicating the irreversible signature of functional group reduction reaction and the SEI formation.[42,66,68,69] Accordingly, the 2nd cycle onwards the cyclic voltammograms revealed three reversible redox peaks for pristine Co-GNP (1.25/1.91 V, 0.71/1.32 V and 0.015/0.21 V), Co-GNP-ZipC (1.20/1.85 V, 0.74/1.26 V and 0.015/0.21 V) and Co-GNP-FmC materials (1.25/1.85 V, 0.72/1.26 V and 0.015/0.21 V). The obtained redox peaks were almost overlapped, and current density increment for the redox process of Li^+ ion intercalation and deintercalation in GNPs (pristine Co-GNP) and the graphitic shell encapsulated carbon (Co-GNP-ZipC and Co-GNP-FmC) could be observed indicating enhancement of Li^+ ion storage, as given in Fig. 4d–f. From the electrochemical kinetic studies (EIS and CV) of Co-GNP-ZipC and Co-GNP-FmC, it is

confirmed that the plastic waste derived graphitic shell encapsulated Co-GNP-ZipC and Co-GNP-FmC materials can be used as superior anodes for Li-ion batteries.

2.5. Plastic waste built graphitic shell encapsulated Co nanoparticles enabled stable Li^+ ion storage

From the confirmed Li^+ ion reversible kinetic studies of pristine Co-GNP, Co-GNP-ZipC and Co-GNP-FmC materials (Fig. 4c–f), the galvanostatic discharge- and charge cycling studies were performed on the fabricated lithium cells (Li *vs.* Co-GNP, Li *vs.* Co-GNP-ZipC and Li *vs.* Co-GNP-FmC) between 0.01 and 2.5 V at 37 mA g^{-1}, assembled with lithium metal, graphitic shell encapsulated Co nanoparticle electrode, Celgard separator and 1 M $LiPF_6$ in EC + DEC (1 : 1 vol%) electrolyte, as depicted in Fig. 5. The voltage *vs.* capacity plateaus revealed two clear flat and sloped voltage regions, delivering the initial reversible capacity of 390 mA h g^{-1} for pristine Co-GNP, 325 mA h g^{-1} for Co-GNP-ZipC and 277 mA h g^{-1} for Co-GNP-FmC materials, associated with two types of Li^+ ion storage reactions: (i) intercalation by graphitic shell encapsulated carbon below 0.25 V (flat) and (ii) conversion by Co nanoparticles above 0.25 V (slope), as shown in Fig. 5a–c. An additional initial flat voltage region between 1.2 and 0.8 V indicated the irreversible reduction reaction of the GNP surface adsorbed functional groups (COOH, CO, O^{2-} and OH^- *etc.*) followed by the electrolyte decomposition reaction (0.8 V), forming SEI and amorphous CoO and Li_2O products, as determined by CV studies (Fig. 4d–f). During continuous cycles, the flat and sloped voltage regions of the pristine Co-GNP material slowly reduced and completely disappeared at the 250th cycle, revealing declined Li^+ ion storage reaction of the graphitic carbon intercalation and the redox process of cobalt metal, as shown in Fig. 5a. In contrast, plastic waste derived Co-GNP-ZipC and Co-GNP-FmC materials revealed quite stable flat and sloped voltage profiles, indicating highly reversible reactions of intercalation by graphitic shell encapsulated carbon (Li_xC) and the Co nanoparticle's conversion reaction ($CoO + 2Li^+ + 2e^- \leftrightarrow Co + Li_2O$), as shown in Fig. 5b and c. Significantly, the gradual reversible capacity

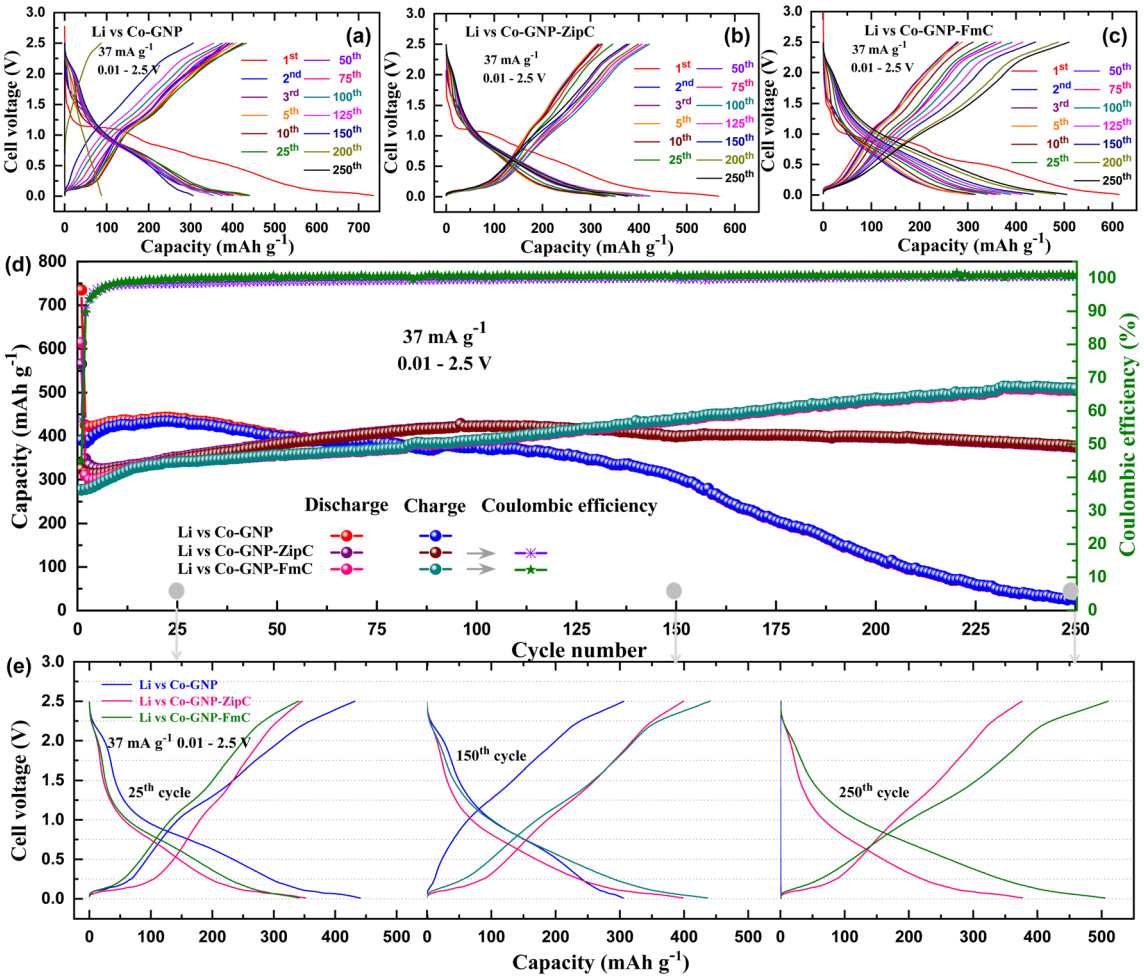

Fig. 5 Galvanostatic cycling studies of pristine and the plastic waste derived graphitic shell encapsulated cobalt nanomaterials: voltage *vs.* capacity performance of lithium cells (a) pristine Li *vs.* Co-GNP, (b) Li *vs.* Co-GNP-ZipC, (c) Li *vs.* Co-GNP-FmC, (d) cycling stability studies between 0.01 and 2.5 V at 37 mA g^{-1} for 1–250 cycles, and (e) voltage profile comparison at the 25th, 150th and 250th cycles for the pristine and the plastic waste derived materials. The lithium cells assembled with the respective electrode (Co-GNP, Co-GNP-ZipC and Co-GNP-FmC), lithium metal foil (~120 μm thickness), Celgard polypropylene separator and 1 M $LiPF_6$ in EC + DEC (1 : 1 vol%) electrolyte.

increment with slope voltage of Co-GNP-ZipC and Co-GNP-FmC materials was associated with the increases of reversible conversion reaction between Li_2O and Co, where nano Co metal acts as a catalyst for Li_2O reversible process (Fig. 5b and c), corroborated by the literature reports.[42,66–69]

For further investigation of cycling stability studies, the discharge–charge capacities of the pristine Co-GNP, Co-GNP-ZipC and Co-GNP-FmC materials were compared between 1 and 250 cycles at 37 mA g^{-1}, as given in Fig. 5d. The lithium cell of the pristine Co-GNP material delivered a higher reversible capacity of 432 mA h g^{-1} at the 25th cycle than the plastic waste derived lithium cells, *viz.*, Li *vs.* Co-GNP-ZipC (346 mA h g^{-1}) and Li *vs.* Co-GNP-FmC (340 mA h g^{-1}). The measured reversible charge capacity of 432 mA h g^{-1} for the pristine Co-GNP was close to the theoretical specific capacity 471 mA h g^{-1}, contributed by graphitic nanoplatelets (71%, 264 mA h g^{-1}) and the formed CoO (~29%, 207 mA h g^{-1}). Notedly, a gradual capacity fade observed between 25^{th} to 150^{th} cycles for pristine Co-GNP and then abruptly decreased the reversible capacity and lost its cycling operation at the 250^{th} cycle without any capacity contribution, as shown in Fig. 5d. On the other hand, the plastic waste derived material revealed the capacity increase, *viz.*, 377 mA h g^{-1} for Co-GNP-ZipC and 509 mA h g^{-1} for Co-GNP-FmC with the coulombic efficiency of 100% at the 250th cycle, which is greater than the pristine Co-GNP material performance, as shown in Fig. 5d. Remarkably, a high reversible capacity of 509 mA h g^{-1} was observed for the Co-GNP-FmC material attributed to the Li^+ ion storage mechanism of (de)insertion in trace amounts of amorphous CoO,[42,66–69] conversion reaction of CoO to Co and Li_2O[42,66–69] and Li^+ ion intercalation in graphitic shell encapsulated carbon.[42,66–69] On further investigation of the cycling studies, it is seen that at the 25th cycle the voltage *vs.* capacity profile of the pristine Co-GNP material for the graphene nanoplates' (de)intercalation and the CoO's conversion reaction (blue, Fig. 5e) was close to that of the plastic waste derived Co-GNP-ZipC (pink) and Co-GNP-FmC materials (green). Next, at the 150th cycle considerable change in the voltage *vs.* capacity profile of the pristine Co-GNP (blue) was observed and then at the 250th cycle the Li^+ ion storage completely dropped, and the voltage curve showed a vertical line (blue), while the graphitic shell encapsulated Co nanoparticle materials delivered higher capacities of 377 mA h g^{-1} for Co-GNP-ZipC (pink) and 509 mA h g^{-1} for Co-GNP-FmC (green), as depicted in Fig. 5e.

The phenomenon of superior Li^+ ion storage at the 250th cycle for the plastic waste derived materials (377 mA h g^{-1} for Co-GNP-ZipC and 509 mA h g^{-1} for Co-GNP-FmC) can be described by graphitic shell encapsulated carbon, acting as a protecting shell during cycling. As shown in Fig. 6a, the pristine Co-GNP material comprised Co nanoparticles and GNPs; after the first lithiation process the formed amorphous CoO nanoparticle could be pulverized into a much smaller size during repeated discharge–charge cycles, as reported in the literature.[67,68] In the voltage *vs.* capacity profile, the lithium cell of the pristine Co-GNP material delivered a reversible capacity of 432 mA h g^{-1} at the 25th cycle (pink) with two types of Li^+ ion storage mechanisms, denoted by the flat and sloped voltage regions (Fig. 6a) corresponding to the GNPs' (de)intercalation and the CoO's conversion reaction. The delivered capacity decreased to 306 mA h g^{-1} at the 150th cycle (green) with gradual decay in capacity; a rapid decay was observed, resulting in declined Li^+ ion storage at the 250th cycle, revealing the voltage profile as a vertical line (blue) with a delivered capacity of <1 mA h g^{-1}, as shown in Fig. 6a. The declined Li^+ ion storage of the pristine material can be attributed to the loose aggregates (CoO) produced, which could have detached from the GNPs due to weak contact, leading to fast decay in capacity and declined redox process.[42,66–69,73] On the other hand, the plastic waste derived materials showed promising Li^+ ion storage at the 250th cycle, 377 mA h g^{-1} for Co-GNP-ZipC and 509 mA h g^{-1} for the Co-GNP-FmC material without any significant changes in capacity and voltage profiles, as given in Fig. 6b and c. After cycling, the surface morphology structure of the pristine Co-GNP and plastic derived Co-GNP-ZipC and Co-GNP-FmC materials was investigated, as shown in Fig. S4.† FESEM images of the pristine Co-GNP material showed electrode disintegration and cracking (Fig. S4a–c†) resulting in declined Li^+ ion storage at the 250th cycle, while plastic derived Co-GNP-ZipC (Fig. S4d–f†) and Co-GNP-FmC (Fig. S4g–i†) materials having graphitic carbon shell encapsulation on the cobalt nanoparticles revealed a stable morphology structure attributed to promising Li^+ ion storage at the 250th cycle, 377 mA h g^{-1} for Co-GNP-ZipC and 509 mA h g^{-1} for Co-GNP-FmC material without any significant changes in capacity and voltage profiles. For this reason, the catalytic microwave plastic waste built a unique Co nanoparticle material with graphitic carbon coupling for high electronic conductivity and mechanical stability towards volume expansion.[37,43,74,75] Thus, the graphitic carbon coupling on Co nanoparticles can promote the charge transfer between graphitic carbon and Co nanoparticles, modifying the electronic and electrochemical properties of plastic waste materials during electrochemical cycling studies for Li^+ ion storage.[37,43] Then, the carbon coupling can act as a barrier to Co nanoparticles, protect from direct electrolyte contact/harsh environments, and prevent unwanted chemical reactions between the electrolyte and amorphous CoO nanoparticles for prolonged phase transformations.[37,43] So, ultrafast graphitic carbon shell encapsulation on cobalt nanoparticles using plastic waste in 2 minutes would be more promising for the creation of core–shell architecture and the applications of ferromagnetism and stable Li^+ ion storage than the heterogeneous processes of microwave techniques.[76–79] The deep dehydrogenation of the hexadecane process is carried out using Fe/SiC catalysts, wherein the catalyst is synthesized by sol–gel and calcination processes (at 350 °C for 3 h) with the microwave irradiation technique.[76,77] Moreover, the production of hydrogen,[78] and catalytic hydrogenation of carbon dioxide[79] do not belong to graphitic shell encapsulation on cobalt nanoparticles for ferromagnetic and long-term lithium-ion battery cycling studies. Thus, the synchronized microwave route comprises the simultaneous process of (i) graphene-triggered cobalt catalyst formation, (ii) catalytic attack on polyolefins' bonds, (iii) plastic waste decomposition, and (iv) core–shell formation of graphitic carbon encapsulation on cobalt nanoparticles in 2 minutes. Eventually, the observed

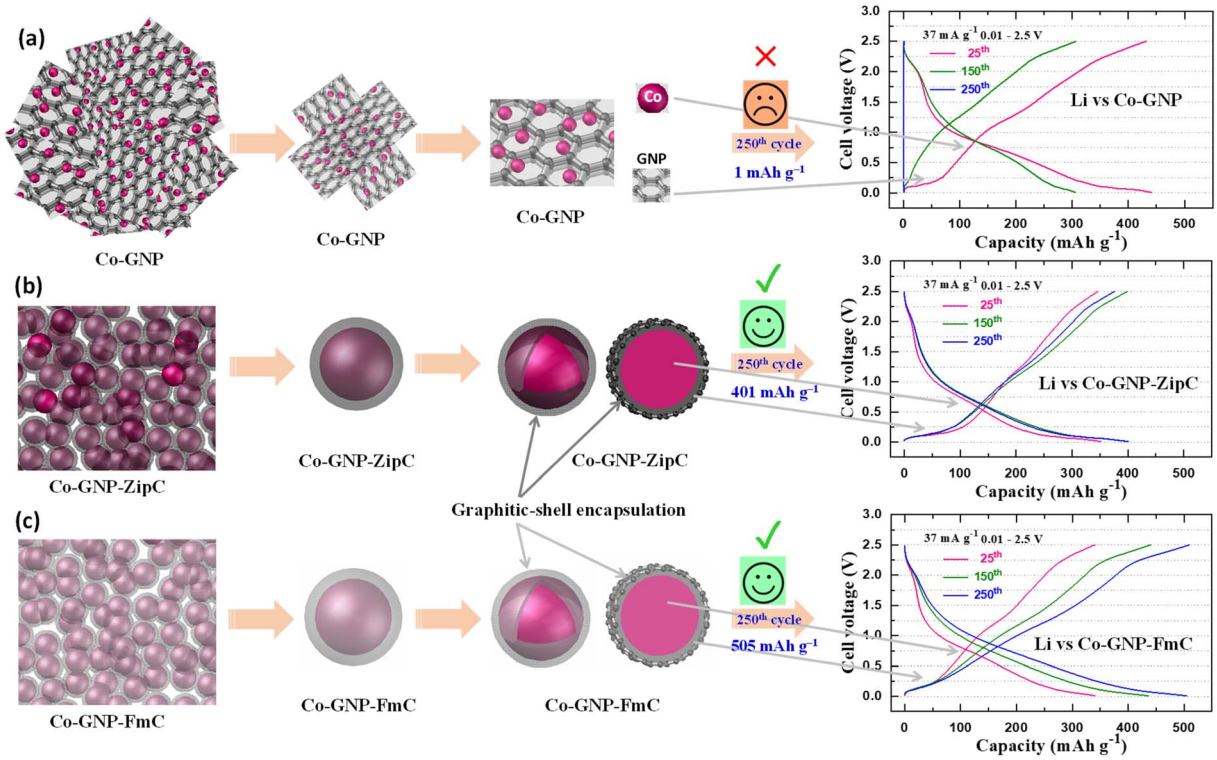

Fig. 6 Enhanced Li^+ ion storage achieved by plastic waste produced core–shell structure: schematic illustration of the (a) pristine Co-GNP material, comprising Co nanoparticles and GNPs, declined Li^+ ion storage at the 250th cycle; (b) polyethylene derived core–shell architecture of the Co-GNP-ZipC material, delivering high charge capacity of 377 mA h g^{-1} at the 250th cycle, and (c) polystyrene derived core–shell architecture of the Co-GNP-FmC material, delivering superior charge capacity of 509 mA h g^{-1} at the 250th cycle (blue). Graphitic shell encapsulation on cobalt nanoparticles reveals a barrier and protects from the direct electrolyte contact and harsh environments for more stability than the pristine Co-GNP.

capacity enhancement of plastic waste-derived materials during cycling can be associated with the incidence of increasing amorphous CoO active sites by forming much smaller amorphous CoO due to repeated discharge–charge cycles and increasing the reversibility of Li_2O by catalytic activation of Co nanoparticles releasing Li^+ ions during cycling, as described in CV and discharge–charge cycling studies. Therefore, at the 250th cycle the plastic waste derived materials sustained the flat and sloped voltage plateaus and yielded a reversible capacity of 377 mA h g^{-1} for Co-GNP-ZipC and 509 mA h g^{-1} for the Co-GNP-FmC material compared to the pristine Co-GNP material (<1 mA h g^{-1}), which manifested as a superior Li^+ ion storage material.

3. Conclusions

In summary, environmentally challenging landfill plastic waste, *viz.*, polyethylene Ziploc bags and polystyrene packing foam, was catalytically deconstructed and produced graphitic shell encapsulated cobalt nanoparticles by the microwave irradiation technique in 2 minutes. The cubic crystal phase purity of the plastic waste-derived materials (Co-GNP-ZipC and Co-GNP-FmC) was confirmed by powder XRD patterns, and the defective graphitic carbon determined by Raman spectroscopic analysis using the D-band at 1330 cm^{-1} and G-band at 1575 cm^{-1} with the comparison of the pristine CO-GNP material. BET studies of surface characteristics revealed H3 and H4-hysteresis loops, and the specific surface area of the plastic waste derived composite materials was calculated to be 39 m^2 g^{-1} for Co-GNP-ZipC, 19 m^2 g^{-1} for Co-GNP-FmC and 47 m^2 g^{-1} for pristine Co-GNP. TEM results obtained confirmed graphitic shell encapsulated cobalt nanoparticles (~20 nm) and showed carbon lattice fringes for the graphitic core–shell architecture and ring patterns with bright diffraction spots for highly crystalline cobalt nanoparticles. The magnetic field dependence of magnetization M *vs.* H and temperature dependence of magnetic susceptibility χ *vs.* T of pristine Co-GNP, Co-GNP-ZipC and Co-GNP-FmC revealed ferromagnetism for the presence of cobalt nanoparticles without any antiferromagnetic phase transition for CoO. Kinetic studies revealed the charge storage buildup of the graphitic core–shell and showed three reversible redox peaks attributed to the Li^+ ion storage mechanisms of (de) insertion in trace amounts of amorphous CoO, conversion reaction of CoO to Co and Li_2O and Li^+ ion (de)intercalation in graphitic shell encapsulated carbon. Plastic waste derived composite materials delivered a high reversible capacity of 377 mA h g^{-1} for Co-GNP-ZipC and 509 mA h g^{-1} for Co-GNP-FmC with the coulombic efficiency of 101% at the 250th cycle compared to the pristine Co-GNP material (<1 mA h g^{-1}) and manifested as superior Li^+ ion storage materials. Significantly, graphitic core–shell architecture shields Co nanoparticles from direct electrolyte contact and harsh environments, and prevents

unwanted chemical reactions between the electrolyte and amorphous CoO nanoparticles for prolonged phase transformations and enhanced Li^+ ion storage.

4. Experimental methods

4.1. Synthesis of ultrafast graphitic shell encapsulated cobalt nanoparticles

Plastic wastes, which are an environmental burden, Ziploc bags (polyethylene), and food packing boxes and packing foam materials (polystyrene) were cut to smaller sizes corresponding to the weight of 350 mg (polystyrene dissolved in acetone and allowed to evaporate naturally) and mixed with 1 millimole of cobalt acetate (Sigma-Aldrich). Subsequently, 43 mg of graphene nanoplatelets (GNPs) were added to the plastic waste mixture and blended to attain maximum homogeneity in a separate round bottom flask (polyethylene and polystyrene). Then, the blended mixture was treated by dry microwave irradiation for 2 minutes and then allowed to naturally cool down, producing 225 mg of ultrafast graphitic shell encapsulated cobalt nanoparticles, as shown in Fig. 1. The black powders obtained were labelled Co-GNP-ZipC for polyethylene plastic waste (Ziploc bag) and Co-GNP-FmC for polystyrene plastic waste (foam). Furthermore, the pristine material was synthesized using a homogenized mixture of cobalt acetate and GNPs, and irradiated for 2 minutes without the plastic waste, which yielded a black Co-GNP powder.

4.2. Physicochemical characterization

The phase purity of the plastic waste derived Co-GNP-ZipC, Co-GNP-FmC and pristine Co-GNP materials was examined by powder XRD analyses using a Rigaku SmartLab X-ray diffractometer, recorded with 2θ between 10 and 80° under the conditions of 40 kV and 40 mA with a Cu Kα X-ray source (λ = 0.154 nm). The graphitic characteristics of the developed composite materials, *viz.*, Co-GNP-ZipC, Co-GNP-FmC and pristine Co-GNP were confirmed by Raman spectroscopy measurements with a laser excitation wavelength of 633 nm using a Thermo Fisher Scientific DXR Raman microscope instrument. To determine dehydration and cobalt acetate decomposition, thermogravimetric analysis (TGA) was performed on the mixture of cobalt acetate and graphene nanoplatelets between 25 °C and 900 °C at 10 °C min^{-1} in an Ar atmosphere using a TGA i-1000 instrument. Surface characteristics of the composite materials (Co-GNP-ZipC, Co-GNP-FmC and pristine Co-GNP) were studied by Brunauer–Emmett–Teller (BET) specific surface area measurements and the N_2 adsorption–desorption isotherm curves, using a NOVA 2200e BET analyzer (Quantachrome Instruments, USA). Moreover, the nanoarchitecture's surface morphology, graphitic shell encapsulation, particle size and crystallinity were investigated by an advanced transmission electron microscopic (TEM) technique (FEI Tecnai F20 S/TEM) with selected area electron diffraction (SAED) patterns, simultaneous elemental mapping analyses, high-angle annular dark field (HAADF) and energy dispersive X-ray analyses, which confirmed the presence of cobalt (Co) and carbon (C) elements. Magnetization and magnetoresistance measurements of the cobalt metal in the graphitic shell encapsulated cobalt nanoparticles (Co-GNP-ZipC and Co-GNP-FmC) and the pristine material (Co-GNP) were examined by SQUID magnetometry for the powder sample in the temperature range of 1.8–300 K at magnetic fields up to 3 T using a Design MPMS SQUID magnetometer in DC mode.

4.3. Electrochemical characterization

The charge transfer resistance of the graphitic shell encapsulated cobalt nanoparticles, electrochemical kinetic characteristics, and Li^+ ion intercalation and deintercalation were investigated by electrochemical impedance spectroscopic (EIS) measurements, cyclic voltammetric (CV) analyses and galvanostatic discharge–charge studies using fabricated lithium cells (Li *vs.* Co-GNP-ZipC and Li *vs.* Co-GNP-FmC) in comparison with the pristine Co-GNP material (Li *vs.* Co-GNP). The lithium cells were assembled with the respective electrode (Co-GNP, Co-GNP-ZipC and Co-GNP-FmC), lithium metal foil (~120 μm thickness), Celgard polypropylene separator and 1 M $LiPF_6$ in EC + DEC (1 : 1 vol%) electrolyte. The electrodes of pristine Co-GNP, plastic waste derived Co-GNP-ZipC and Co-GNP-FmC materials were fabricated using an MTI laminate coater by the doctor-blade method. The homogenized electrode slurry mixture was prepared using a Thinky planetary mixer, with the composition of 80% active material, 10% super carbon and 10% polyvinylidene binder dissolved in *N*-methyl-2-pyrrolidone solvent, coated on a copper foil current collector and dried at 80 °C for 15 h in a vacuum oven. After drying, the dried electrodes were calendered by roll pressing and the electrode was cut to the size of 14 mm diameter using a disc cutter, containing a load of ~3 mg (wt). The lithium cells were assembled in a glovebox (NEXUS II Vacuum Atmospheres Co), filled with argon, and the moisture level (O_2 and H_2O) was controlled at <0.5 ppm. EIS analyses were performed on the fabricated lithium cells to examine the charge transfer resistance and the kinetic characteristics in the plastic waste derived Co-GNP-ZipC and Co-GNP-FmC materials using a Gamry instrument (Reference-600) in the frequency range of 1 MHz to 25 mHz at 10 mV amplitude. Then, the electrochemical kinetic reversibility of Li^+ ion intercalation–deintercalation characteristics was investigated by cyclic voltammetric (CV) analysis using a Gamry instrument at the scan rate of 0.1 mV s^{-1} between 0.01 and 2.5 V for 1–5 cycles. The galvanostatic discharge–charge cycling studies of pristine Co-GNP, Co-GNP-ZipC and Co-GNP-FmC composite material were performed using an ARBIN cycler (Model BT2043) at 25 °C in the voltage range of 0.01–2.5 V at 37 mA g^{-1}.

Conflicts of interest

The authors declare no conflict of interest.

Acknowledgements

The authors thank Davidson School of Chemical Engineering at Purdue University for financial support.

References

1 D. E. MacArthur, *Science*, 2017, **358**, 843.
2 R. Geyer, J. R. Jambeck and K. L. Law, *Sci. Adv.*, 2017, **3**, 25–29.
3 G. Lopez, M. Artetxe, M. Amutio, J. Bilbao and M. Olazar, *Renewable Sustainable Energy Rev.*, 2017, **73**, 346–368.
4 D. S. Achilias, C. Roupakias, P. Megalokonomos, A. A. Lappas and V. Antonakou, *J. Hazard. Mater.*, 2007, **149**, 536–542.
5 B. I. Yun, *J. Comput. Appl. Math.*, 2011, **235**, 1553–1555.
6 S. L. Wong, N. Ngadi, T. A. T. Abdullah and I. M. Inuwa, *Renewable Sustainable Energy Rev.*, 2015, **50**, 1167–1180.
7 C. Wu, M. A. Nahil, N. Miskolczi, J. Huang and P. T. Williams, *Environ. Sci. Technol.*, 2014, **48**, 819–826.
8 A. Erkiaga, G. Lopez, I. Barbarias, M. Artetxe, M. Amutio, J. Bilbao and M. Olazar, *J. Anal. Appl. Pyrolysis*, 2015, **116**, 34–41.
9 S. M. Hong, H. J. Yoon, Y. Choi, Y. Z. Cho, S. Mun, V. G. Pol and K. B. Lee, *Chem. Eng. J.*, 2020, **379**, 122219.
10 M. H. Kim, J. Tang, S. J. Jang, V. G. Pol and K. C. Roh, *J. Alloys Compd.*, 2019, **805**, 1282–1287.
11 S. Villagómez-Salas, P. Manikandan, S. F. Acuña Guzmán and V. G. Pol, *ACS Omega*, 2018, **3**, 17520–17527.
12 T. Uekert, M. F. Kuehnel, D. W. Wakerley and E. Reisner, *Energy Environ. Sci.*, 2018, **11**, 2853–2857.
13 J. Chen, J. Wu, P. C. Sherrell, J. Chen, H. Wang, W. xian Zhang and J. Yang, *Adv. Sci.*, 2022, **9**, 1–36.
14 B. Dou, K. Wang, B. Jiang, Y. Song, C. Zhang, H. Chen and Y. Xu, *Int. J. Hydrogen Energy*, 2016, **41**, 3803–3810.
15 I. Barbarias, G. Lopez, J. Alvarez, M. Artetxe, A. Arregi, J. Bilbao and M. Olazar, *Chem. Eng. J.*, 2016, **296**, 191–198.
16 S. Czernik and R. J. French, *Energy Fuel.*, 2006, **20**, 754–758.
17 M. A. Nahil, C. Wu and P. T. Williams, *Fuel Process. Technol.*, 2015, **130**, 46–53.
18 D. Yao, Y. Zhang, P. T. Williams, H. Yang and H. Chen, *Appl. Catal., B*, 2018, **221**, 584–597.
19 R. X. Yang, K. H. Chuang and M. Y. Wey, *RSC Adv.*, 2016, **6**, 40731–40740.
20 J. C. Acomb, C. Wu and P. T. Williams, *Appl. Catal., B*, 2016, **180**, 497–510.
21 P. J. Kim, H. D. Fontecha, K. Kim and V. G. Pol, *ACS Appl. Mater. Interfaces*, 2018, **10**, 14827–14834.
22 S. Kang, H. Choi, S. Bin Lee, S. C. Park, J. B. Park, S. Lee, Y. Kim and B. H. Hong, *2D Mater.*, 2017, **4**(1–7), 0250317.
23 D. E. Clark, D. C. Folz and J. K. West, *Mater. Sci. Eng., A*, 2000, **287**, 153–158.
24 C. Yang, H. Yang, Y. Bai, X. Wu, W. Guo, M. Li, F. Zhang, P. F. Wang and X. Han, *Energy Fuel.*, 2021, **35**, 898–904.
25 C. Wang, X. Han, P. Xu, X. Zhang, Y. Du, S. Hu, J. Wang and X. Wang, *Appl. Phys. Lett.*, 2011, **98**, 1–4.
26 H. Lv, Y. Guo, Z. Yang, Y. Cheng, L. P. Wang, B. Zhang, Y. Zhao, Z. J. Xu and G. Ji, *J. Mater. Chem. C*, 2017, **5**, 491–512.
27 M. Cao, C. Han, X. Wang, M. Zhang, Y. Zhang, J. Shu, H. Yang, X. Fang and J. Yuan, *J. Mater. Chem. C*, 2018, **6**, 4586–4602.
28 F. Meng, H. Wang, F. Huang, Y. Guo, Z. Wang, D. Hui and Z. Zhou, *Composites, Part B*, 2018, **137**, 260–277.
29 Y. Li, S. Zhang and Y. Ni, *Mater. Res. Express*, 2016, **3**(1–13), 075012.
30 A. A. Balandin, S. Ghosh, W. Bao, I. Calizo, D. Teweldebrhan, F. Miao and C. N. Lau, *Nano Lett.*, 2008, **8**, 902–907.
31 S. E. Lee, O. Choi and H. T. Hahn, *J. Appl. Phys.*, 2008, **104**(1–8), 033705.
32 S. Vinayasree, M. A. Soloman, V. Sunny, P. Mohanan, P. Kurian and M. R. Anantharaman, *Compos. Sci. Technol.*, 2013, **82**, 69–75.
33 X. Zhao, Z. Zhang, L. Wang, K. Xi, Q. Cao, D. Wang, Y. Yang and Y. Du, *Sci. Rep.*, 2013, **3**, 1–5.
34 D. Micheli, A. Vricella, R. Pastore and M. Marchetti, *Carbon*, 2014, **77**, 756–774.
35 X. X. Liu, J. B. Zang, L. Chen, L. B. Chen, X. Chen, P. Wu, S. Y. Zhou and Y. H. Wang, *J. Mater. Chem. A*, 2017, **5**, 5865–5872.
36 X. Yan, C. L. Dong, Y. C. Huang, Y. Jia, L. Zhang, S. Shen, J. Chen and X. Yao, *Small Methods*, 2019, **3**, 1–7.
37 H. Khani, N. S. Grundish, D. O. Wipf and J. B. Goodenough, *Adv. Energy Mater.*, 2020, **10**, 1–10.
38 J. Lu, W. Zhou, L. Wang, J. Jia, Y. Ke, L. Yang, K. Zhou, X. Liu, Z. Tang, L. Li and S. Chen, *ACS Catal.*, 2016, **6**, 1045–1053.
39 X. Chen, J. Xiao, J. Wang, D. Deng, Y. Hu, J. Zhou, L. Yu, T. Heine, X. Pan and X. Bao, *Chem. Sci.*, 2015, **6**, 3262–3267.
40 X. Cui, P. Ren, D. Deng, J. Deng and X. Bao, *Energy Environ. Sci.*, 2016, **9**, 123–129.
41 H. Park, K. Kim, K. Jeong, J. S. Kang, H. H. Cho, B. Thirumalraj, Y. E. Sung, H. N. Han, J. H. Kim, D. C. Dunand and H. Choe, *Appl. Surf. Sci.*, 2020, **525**, 146592.
42 V. Etacheri, C. N. Hong, J. Tang and V. G. Pol, *ACS Appl. Mater. Interfaces*, 2018, **10**, 4652–4661.
43 P. Nie, Z. Le, G. Chen, D. Liu, X. Liu, H. Bin Wu, P. Xu, X. Li, F. Liu, L. Chang, X. Zhang and Y. Lu, *Small*, 2018, **14**, 1–8.
44 M. Palanisamy, V. G. Pol, S. F. Evans, K. Jackson, C. J. Jafta, C. A. Bridges, S. Dai, A. M. Levine, R. J. Lee and M. P. Paranthaman, *Sustain. Energy Fuels*, 2020, **4**, 3613–3622.
45 M. G. Park, D. H. Lee, H. Jung, J. H. Choi and C. M. Park, *ACS Nano*, 2018, **12**, 2955–2967.
46 P. Manikandan, P. Periasamy and R. Jagannathan, *RSC Adv.*, 2015, **5**, 3844–3853.
47 G. Huang, S. Xu, S. Lu, L. Li and H. Sun, *ACS Appl. Mater. Interfaces*, 2014, **6**, 7236–7243.
48 J. Zhou, C. Zheng, H. Wang, J. Yang, P. Hu and L. Guo, *Nanoscale*, 2016, **8**, 17131–17135.
49 Z. Yi, Q. Han, P. Zan, Y. Cheng, Y. Wu and L. Wang, *J. Mater. Chem. A*, 2016, **4**, 12850–12857.
50 J. Wang, J. Kim, S. Choi, H. Wang and J. Lim, *Small Methods*, 2020, **4**, 1–22.
51 J. H. Jang, A. A. Jeffery, J. Min, N. Jung and S. J. Yoo, *Nanoscale*, 2021, **13**, 15116–15141.
52 S. J. Goldie, S. Jiang and K. S. Coleman, *Mater. Adv.*, 2021, **2**, 3353–3361.

53 X. Jie, W. Li, D. Slocombe, Y. Gao, I. Banerjee, S. Gonzalez-Cortes, B. Yao, H. AlMegren, S. Alshihri, J. Dilworth, J. Thomas, T. Xiao and P. Edwards, *Nat. Catal.*, 2020, **3**, 902–912.
54 M. J. Xiao, B. Ma, Z. Q. Zhang, Q. Xiao, X. Y. Li, Z. T. Zhang, Q. Wang, Y. Peng and H. L. Zhang, *J. Mater. Chem. A*, 2021, **9**, 7227–7237.
55 M. Palanisamy, C. Jamison, X. Sun, Z. Qi, H. Wang and V. G. Pol, *Carbon*, 2021, **185**, 608–618.
56 M. Agostini, L. G. Rizzi, G. Cesareo, V. Russo and J. Hassoun, *Adv. Mater. Interfaces*, 2015, **2**, 1–7.
57 W. S. Jiang, C. Yang, G. X. Chen, X. Q. Yan, S. N. Chen, B. W. Su, Z. B. Liu and J. G. Tian, *J. Mater. Chem. C*, 2018, **6**, 1829–1835.
58 K. S. W. Sing and R. T. Williams, *Adsorpt. Sci. Technol.*, 2004, **22**, 773–782.
59 M. Thommes, *Chem. Ing. Tech.*, 2010, **82**, 1059–1073.
60 M. Palanisamy, R. Perumal and V. G. Pol, *ACS Appl. Mater. Interfaces*, 2022, **14**, 684–697.
61 C. Y. Chen, N. W. Pu, Y. M. Liu, S. Y. Huang, C. H. Wu, M. Der Ger, Y. J. Gong and Y. C. Chou, *Composites, Part B*, 2017, **114**, 395–403.
62 R. Skomski and J. M. D. Coey, *Permanent Magnetism*, Taylor and Francis, London, 1999.
63 Q. Li, H. Li, V. G. Pol, I. Bruckental, Y. Koltypin, J. Calderon-Moreno, I. Nowik and A. Gedanken, *New J. Chem.*, 2003, **27**, 1194–1199.
64 S. A. Majetich, J. H. Scott, E. M. Kirkpatrick, K. Chowdary, K. Gallagher and M. E. McHenry, *Nanostruct. Mater.*, 1997, **9**, 291–300.
65 M. Palanisamy, M. H. Parekh and V. G. Pol, *Adv. Funct. Mater.*, 2020, **30**, 1–14.
66 A. K. Rai, L. T. Anh, J. Gim and J. Kim, *Ceram. Int.*, 2013, **39**, 9325–9330.
67 Q. An, X. Sun, Y. Na, S. Cai and C. Zheng, *Chin. Chem. Lett.*, 2023, **34**, 107305.
68 F. Li, Q. Q. Zou and Y. Y. Xia, *J. Power Sources*, 2008, **177**, 546–552.
69 G. X. Wang, Y. Chen, K. Konstantinov, M. Lindsay, H. K. Liu and S. X. Dou, *J. Power Sources*, 2002, **109**, 142–147.
70 Y. Lin, J. Huang, L. Shi, G. Cong, C. Zhu and J. Xu, *Nanotechnol. Rev.*, 2020, **9**, 1227–1236.
71 L. Luo, J. Wu, J. Xu and V. P. Dravid, *ACS Nano*, 2014, **8**, 11560–11566.
72 Y. Lu, L. Yu and X. W. Lou, *Chem*, 2018, **4**, 972–996.
73 Y. Sun, X. Hu, W. Luo and Y. Huang, *J. Phys. Chem. C*, 2012, **116**, 20794–20799.
74 J. Wang, W. Wu, H. Kondo, T. Fan and H. Zhou, *Nanotechnology*, 2022, **33**(1–27), 342002.
75 H. Hu, Z. Zhao, Q. Zhou, Y. Gogotsi and J. Qiu, *Carbon*, 2012, **50**, 3267–3273.
76 X. Jie, J. Wang, S. Gonzalez-Cortes, B. Yao, W. Li, Y. Gao, J. R. Dilworth, T. Xiao and P. P. Edwards, *JACS Au*, 2021, **1**, 2021–2032.
77 X. Jie, J. R. Chen, T. Biddle, D. R. Slocombe, J. R. Dilworth, T. Xiao and P. P. Edwards, *Chem. Mater.*, 2022, **34**, 4682–4693.
78 S. Aldrees, S. Gonzalez-Cortes, S. A. Shihri, J. R. Dilworth and P. P. Edwards, *IOP Conf. Ser. Earth Environ. Sci.*, 2023, **1167**(1–11), 012045.
79 L. Cui, C. Liu, B. Yao, P. P. Edwards, T. Xiao and F. Cao, *Front. Chem.*, 2022, **10**, 1–25.